

Large Rashba parameter for 4d strongly correlated perovskite oxide SrNbO₃ ultrathin films

Hikaru Okuma*, Yumiko Katayama, and Kazunori Ueno
Department of Basic Science, University of Tokyo,
Meguro, Tokyo 153-8902, Japan
*hikaruokuma613@g.ecc.u-tokyo.ac.jp

Abstract

To elucidate the spin relaxation mechanism of SrNbO₃ (SNO) ultrathin films, the transport properties of a series of SNO films with various thicknesses t were measured on both sides of the metal-insulator transition. The spin-orbit scattering time (τ_{so}) was deduced from the analysis of the magnetoresistance with weak antilocalization theory, and it was found that τ_{so} was inversely proportional to the momentum scattering time. This result was explained in terms of the D'Yakonov-Perel' mechanism, indicative of the dominant Rashba effect. The values of the Rashba parameter were on the order of 1×10^{-12} eVm, which were largest in the values reported for other ultrathin films of metallic oxides.

Electron systems lacking inversion symmetry show Rashba-type spin-orbit coupling (SOC) [1] [2]. Heterointerfaces with large Rashba SOC [3] [4] [5] [6] have attracted considerable attention due to their potential spintronics applications and intriguing phenomena, such as the intrinsic spin Hall effect [7]. For spintronics, semiconductor heterointerfaces with large Rashba SOC have been used to control spin precession in spin field effect transistors [8] [9]. Recently, a remarkably high spin-to-charge conversion rate [10] was reported for an oxide heterointerface with a large Rashba SOC, which is much larger than those of other Rashba systems, such as an interface between Ag and Bi (Ag/Bi) [11], a surface of a topological insulator α -Sn [12], and heavy metals [13]. Among all systems with Rashba SOC, oxide materials were air stable and easy to fabricate, but their Rashba parameters α_R were smaller than those of other systems with heavy elements. There has been a lot of effort spent finding oxide semiconductor heterostructures with large α_R , such as SrTiO₃ (STO) [14] [15] [16] and KTaO₃ (KTO) [17] [18] based interfaces, all of which use high mobility oxide semiconductors STO or KTO. Furthermore, there have been several reports on α_R for metallic oxide ultrathin films, such as SrIrO₃ (SIO) [19] and La_{2/3}Sr_{1/3}MnO₃ (LSMO) [20], although α_R was even smaller for these materials than for semiconductor heterostructures. Ultrathin films are advantageous over interfaces because information about the electronic structure and local density of states can be directly obtained by using angle-resolved photoemission and scanning tunneling spectroscopy, respectively.

SrNbO₃ (SNO) has the same perovskite-type structure as STO but with a heavier transition metal Nb and a $4d^1$ electronic configuration for niobium, thus exhibiting metallic behavior. Bulk SNO is not stable under ambient conditions. Therefore, recently, SNO thin films were deposited on perovskite substrates in vacuo and have been intensively studied [21] [22] [23]. Since Sr(Ti_{1-x}Nb_x)O₃ ($x=0.02-0.2$) showed a systematic enhancement in the SOC strength with increasing Nb concentration [24] [25], SNO is a potential candidate for a Rashba interface with a high α_R . However, two important issues must be addressed; one issue is that SNO films on semiconductor STO or KTO substrates could show parallel conduction between the SNO film and an oxide-deficient surface of the substrate. Since the doped substrate surface shows high mobility at low temperature, it is difficult to separate the intrinsic SNO and the substrate contributions. Another issue is that the study on Sr(Ti_{1-x}Nb_x)O₃ assumed a D'Yakonov-Perel' (DP)-type spin relaxation mechanism to estimate α_R [25], but there are other possible spin relaxation mechanisms. Thus, we must confirm that the DP-type mechanism dominates the spin relaxation in the SNO film.

Three types of spin relaxation mechanisms have been found for conductive electrons: Elliot-Yafet (EY) type, DP type and Bir-Aronov-Pikus (BAP) type [26]. The EY mechanism describes the spin inversion caused by the momentum scattering of an electron from

impurities and phonons. This spin inversion originates from an entanglement of spin-up and spin-down states caused by the SOC of lattice ions. Therefore, the spin relaxation time (τ_{so}) is proportional to the momentum scattering time (τ_p). The DP mechanism originates from spin precession processes with elastic scattering events. Rashba SOC lifts the spin degeneracy, and then spin-up and spin-down bands have different energies. This is equivalent to having a momentum-dependent internal magnetic field, by which spin processes occur. Momentum scattering causes fluctuations in the internal magnetic field and interrupts spin precession. Therefore, τ_{so} is inversely proportional to τ_p , in contrast to the behavior of the EY mechanism. The BAP mechanism originates from an electron–hole exchange interaction, while SNO is a d^1 metal and only has electrons on the Fermi surface. Thus, this mechanism can be disregarded for SNO films.

In this study, we examine the spin relaxation mechanism of SNO ultrathin films deposited on an insulator substrate. From the analysis of the magnetoresistance (MR) with weak antilocalization (WAL) theory for a series of films with different thicknesses (t) and disorder, we find that τ_{so} is inversely proportional to τ_p , indicating DP-type spin relaxation and a dominant Rashba effect. The values of α_R are on the order of 1×10^{-12} eVm, which are larger than the values reported for other ultrathin films of metallic oxides.

The SNO thin films are fabricated on insulator (001)-oriented $(\text{LaAlO}_3)_{0.3}(\text{Sr}_2\text{AlTaO}_6)_{0.7}$ (LSAT) substrate by a pulsed laser deposition method in vacuo with a back pressure of 10^{-7} Torr at 900 °C. A ceramic target composed of $\text{Sr}_2\text{Nb}_2\text{O}_7$ is ablated by a KrF excimer laser ($\lambda = 248$ nm) with a repetition rate of 5 Hz and an energy fluence of 0.93–1.14 J/cm². The crystal structures of SNO (001) thin films are examined by an out-of-plane $2\theta/\omega$ scan and reciprocal space mapping with X-ray diffraction (Rigaku, Smart Lab). The film thickness is determined by a surface profiler (Bruker, Dektak XT) and a deposition rate. The surface uniformity is estimated with an atomic force microscope (AFM). The transport properties are examined by using four-terminal resistance and Hall resistance measurements in a Physical Properties Measurement System (Quantum Design, PPMS) from 2 to 300 K and –2 to 2 T.

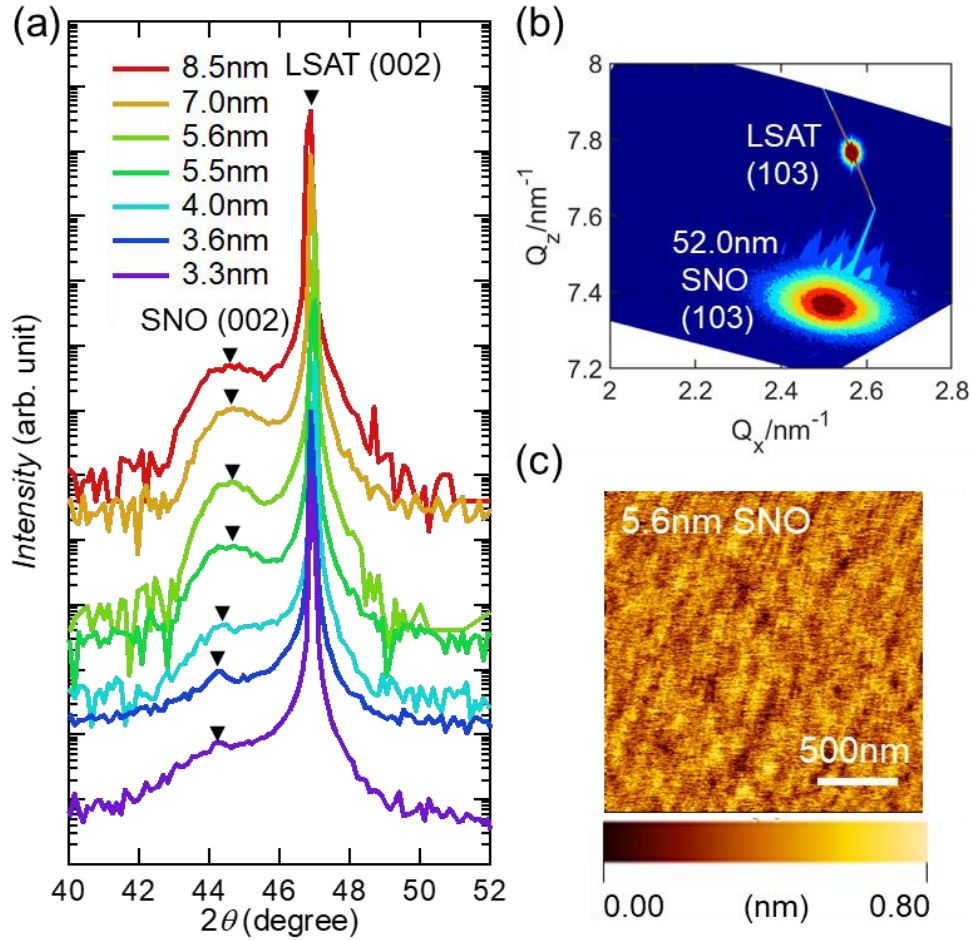


FIG. 1 (a) Out-of-plane $2\theta/\omega$ scan of representative SNO/LSAT with various t values ranging from 3.3 to 8.5 nm. (b) Reciprocal space mapping on a (103) reflection of SNO/LSAT with $t = 52.0$ nm. (c) AFM surface morphology of SNO/LSAT with $t = 5.6$ nm.

Figure 1(a) shows an out-of-plane $2\theta/\omega$ scan of the SNO films on the LSAT substrates (SNO/LSAT) ($a = 0.3868$ nm) with t ranging from 3.3 to 8.5 nm. The out-of-plane lattice constant ranged from 4.050 to 4.094 Å, which was always larger than the lattice constant in a pseudocubic approximation ($a = 4.023$ Å) [27] and is in agreement with a previous report on a SNO film [21]. The crystal structure was directly examined by performing reciprocal space mapping (RSM) on a (103) reflection of SNO/LSAT with $t = 52.0$ nm, as shown in Fig. 1(b). The in-plane and out-of-plane lattice constants were obtained as 3.980 and 4.073 Å, respectively. The cell volume of the SNO film was smaller than that of bulk SNO by approximately 1%, probably indicating small off-stoichiometry variations for the film. The smaller in-plane lattice constant indicates that the film was partly strained by the substrate. Figure 1(c) displays the surface morphology of SNO/LSAT with $t = 5.6$ nm obtained by AFM.

The root mean square (RMS) roughnesses of SNO/LSAT with t ranging from 3.3 to 8.5 nm were always less than 1 nm, indicating that the SNO films had flat surfaces.

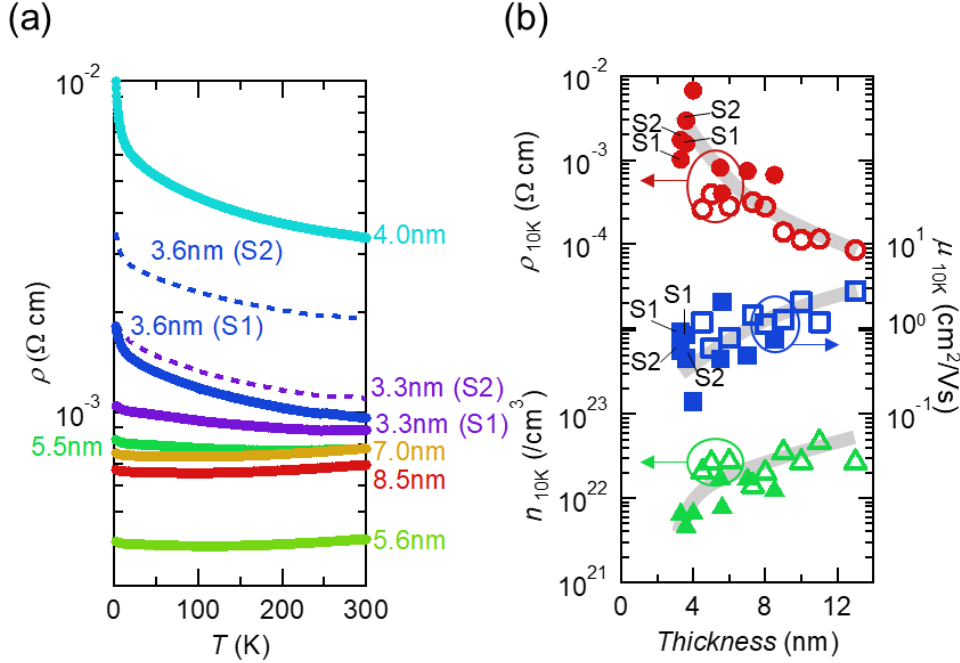


FIG. 2. (a) Temperature dependence of resistivity (ρ) for films with various t values ranging from 3.3 to 8.5 nm. (b) ρ , carrier density (n), and mobility (μ) at 10 K (ρ_{10K} , n_{10K} , and μ_{10K}) plotted against t for films with t ranging from 3.3 to 13 nm. Solid and open symbols correspond to the data for the films indicated in Fig. 2(a) and others not shown in (a), respectively. The dotted lines are visual references.

We examined the temperature dependence of the transport properties of SNO/LSAT films with various t values. Figure 2(a) shows the resistivity (ρ) of the films shown in Fig. 1(a). We observed a metal to insulator (or bad metal) transition (MIT) of the SNO films by reducing t . Films thicker than 4.0 nm exhibited metallic behavior with a resistivity minimum at a certain temperature T_{\min} , which increased with decreasing t . In contrast, the films with $t \leq 4.0$ nm exhibited insulating (or bad metal) behavior over the entire temperature range. We obtained the carrier density (n) from the Hall resistance measurements and the mobility (μ) from ρ and n . In Fig. 2(b), we plotted ρ , n , and μ at 10 K (denoted as ρ_{10K} , n_{10K} , and μ_{10K} , respectively) for the films shown in Fig. 2(a) and others not shown in Fig. 2(a), which are indicated by solid and open symbols, respectively, against t ranging from 3.3 to 13 nm. ρ_{10K} increased by nearly two orders of magnitude with decreasing t , while both n_{10K} and μ_{10K} decreased by nearly one order of magnitude with decreasing t . These results indicate that both an increase in disorder and a decrease in carrier density are responsible for the insulating behavior of the thinner

films with $t \leq 4.0$ nm. Moreover, we noticed the scattering of the data points of ρ_{10K} , n_{10K} , and μ_{10K} in proximity to the individual dotted lines drawn as visual references. This is probably due to the difference in the disorder of the films with a given thickness, such as disorder originating from oxygen vacancies, defects, and surface degradation.

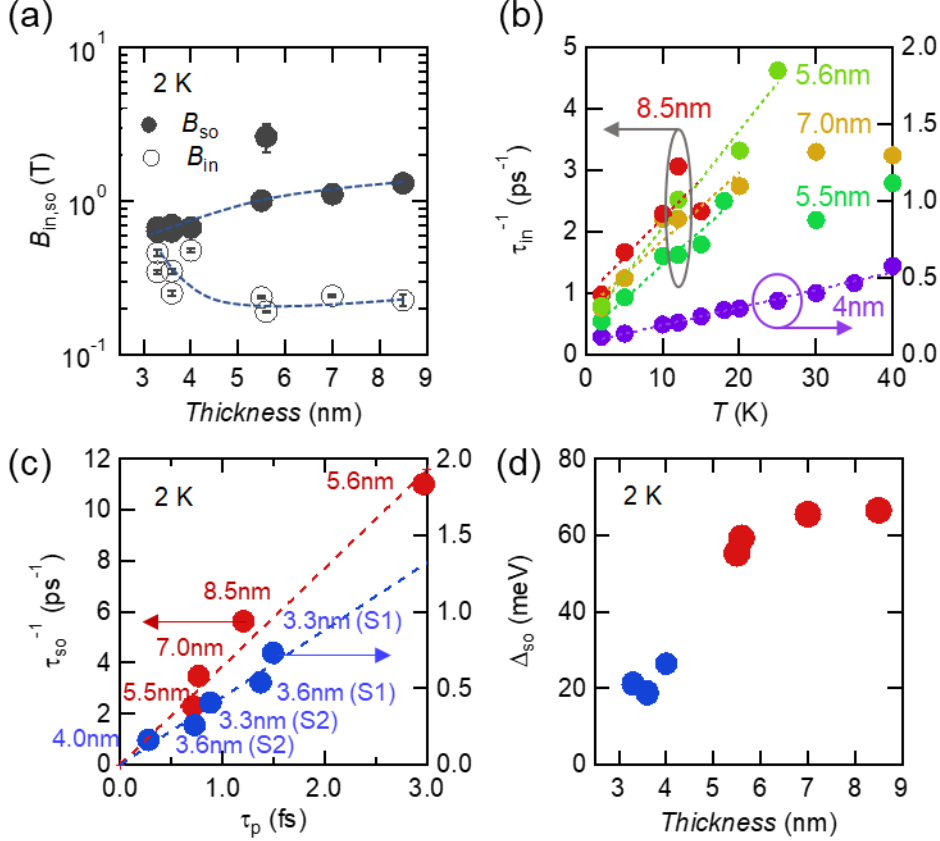


FIG. 3 (a) Effective fields B_{in} (gray solid circles) and B_{so} (gray open circles) extracted from the MR fits at 2 K to Eq. (4) plotted against t . The dotted lines are visual references. (b) Inverse of the inelastic scattering time (τ_{in}^{-1}) at 2 K for the films with t ranging from 4 to 8.5 nm as a function of T . The dotted straight lines represent the linear fits. (c) Inverse of the spin relaxation time (τ_{so}^{-1}) versus the momentum scattering time (τ_p) at 2 K for the films with t ranging from 5.5 to 8.5 nm (red solid circles) and 3.3 to 4.0 nm (blue solid circles). The dashed straight lines are fits of the data to $\tau_{so}^{-1} \propto \tau_p$. The relation $\tau_{so}^{-1} \propto \tau_p$ clearly indicates that the DP spin relaxation mechanism is dominant in the SNO films rather than the EY spin relaxation mechanism, which follows $\tau_{so} \propto \tau_p$. (d) Energy band splitting due to SOC (Δ_{so}) extracted from the data in (c) using Eq. (9) plotted as a function of t .

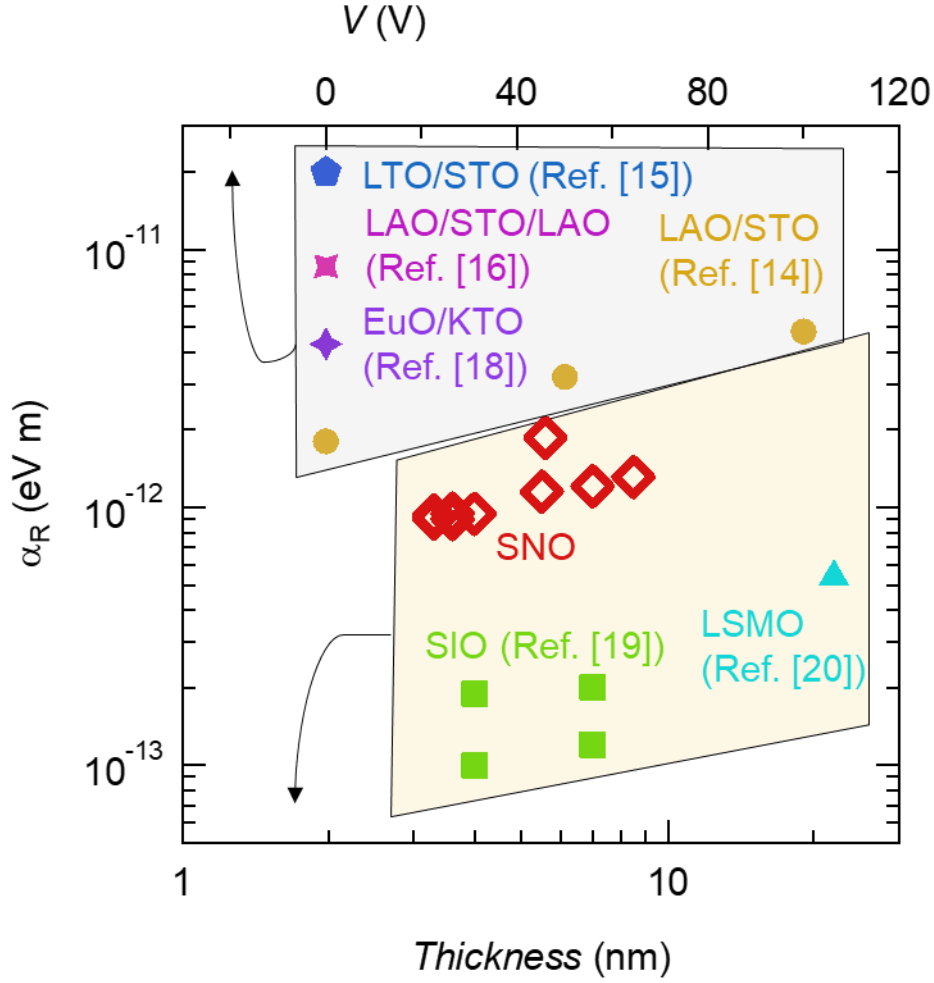


FIG. 4 Rashba parameter (α_R) for oxide materials with metallic films (SNO/LSAT, SIO/STO [19], LSMO/STO [20]) and interface heterostructures (LaAlO₃(LAO)/STO [14], LaTiO₃(LTO)/STO [15], LAO/STO/LAO [16], EuO/KTO [18]).

To estimate the SOC strength, we measured ρ for the films shown in Fig. 1(a) as a function of a perpendicular magnetic field (B) at 2 K. These data are shown in the form of a magnetoconductance $\Delta\sigma(B)$ ($\equiv\sigma(B) - \sigma(0)$) in the Supplemental Material, Sec. A and B [28]. All films showed a positive MR, and $\Delta\sigma(B)$ was well reproduced by WAL theory for a weakly disordered film. We fitted $\Delta\sigma(B)$ both with Hikami-Larkin-Nagaoka (HLN) theory, taking into account the EY spin-relaxation mechanism, and Iordanskii-Lyanda-Pikus (ILP) theory, taking into account the DP spin-relaxation mechanism. In HLN theory, MR is described by the following equation [29] [30]:

$$\frac{\Delta\sigma(B)}{\sigma_0} = - \left[\Psi \left(\frac{1}{2} + \frac{(\hbar/4eL_p^2)}{B} \right) - \ln \left(\frac{\hbar/4eL_p^2}{B} \right) - \Psi \left(\frac{1}{2} + \frac{B_{in} + B_{so}}{B} \right) + \ln \frac{B_{in} + B_{so}}{B} \right], \quad (1)$$

$$L_p = \frac{\hbar k_F \mu}{e}, \quad (2)$$

$$k_F = \sqrt{2n_s \pi}, \quad (3)$$

where $\sigma_0 = e^2/\pi\hbar$, e is the elementary charge, Ψ is the digamma function, \hbar is the Planck constant, L_p is the momentum scattering length, B_{in} and B_{so} are effective fields related to inelastic and spin-orbit scattering, respectively (for details, see below), k_F is the Fermi wavenumber, and n_s is the sheet carrier density. As shown in Fig. S1 in the Supplemental Material, Sec. A [26], $\Delta\sigma(B)$ at 2 K for films with $t = 3.3$ and 4.0 nm followed Eq. (1); however, the values of L_p extracted from the fitting were nearly two orders of magnitude larger than those obtained from k_F and μ . Therefore, it is unlikely that the B dependence of the MR is explained by HLN theory taking into account the EY spin-relaxation mechanism.

Next, we focus on ILP theory, which describes the MR with the following equation [31] [32]:

$$\frac{\Delta\sigma(B)}{\sigma_0} = - \left[\frac{1}{2} \Psi \left(\frac{1}{2} + \frac{B_{in}}{B} \right) - \frac{1}{2} \ln \frac{B_{in}}{B} - \Psi \left(\frac{1}{2} + \frac{B_{in} + B_{so}}{B} \right) + \ln \frac{B_{in} + B_{so}}{B} - \frac{1}{2} \Psi \left(\frac{1}{2} + \frac{B_{in} + 2B_{so}}{B} \right) + \frac{1}{2} \ln \frac{B_{in} + 2B_{so}}{B} \right], \quad (4)$$

As shown in Fig. S2 in the Supplemental Material, Sec. B [26], $\Delta\sigma(B)$ at 2 K followed Eq. (4) for films with t ranging from 3.3 to 8.5 nm. Figure 3(a) shows the t dependence of B_{in} and B_{so} deduced from the fitting by Eq. (4). It was found that B_{so} was always larger than B_{in} , indicating that spin-orbit scattering was dominant over inelastic scattering. With a decrease in t to 5.5 nm, B_{so} decreased gradually, while B_{in} remained nearly constant. With a further decrease in t , B_{in} increased and was comparable to B_{so} for $t \leq 4.0$ nm. This result implies that inelastic scattering was enhanced as the system entered the insulating (bad metal) regime, and then the contribution of inelastic scattering was comparable to that of spin-orbit scattering.

Then, we examined the three characteristic times (inelastic scattering time (τ_{in}), τ_{so} , and τ_p) for the SNO films. B_{in} and B_{so} are related to an inelastic scattering length (time) L_{in} (τ_{in}) and a spin-orbit scattering length (time) L_{so} (τ_{so}), respectively, with the following equations:

$$B_{in,so} = \frac{\hbar}{4eL_{in,so}^2}, \quad (5)$$

$$L_{in,so} = \sqrt{D\tau_{in,so}}, \quad (6)$$

$$D = \frac{1}{2} v_F^2 \tau_p, \quad (7)$$

$$\tau_p = \frac{\mu m}{e}, \quad (8)$$

where D is the diffusion constant, v_F is the Fermi velocity, and m is the effective mass. We employed $m = 2.76m_0$ [22] for all films, where m_0 is the free electron mass. Figure

3(b) displays the inverse of the inelastic scattering time (τ_{in}^{-1}) as a function of T for various films. The linear relation between τ_{in}^{-1} and T was observed and was well explained assuming that electron-electron scattering was dominant [33] [34].

Figure 3(c) shows τ_{so}^{-1} as a function of τ_p for films $t \geq 5.5$ nm (metallic films, red solid circles) and those with $t \leq 4.0$ nm (insulating films, blue solid circles). For both the metallic and insulating films, τ_{so}^{-1} was proportional to τ_p , verifying that the main spin relaxation mechanism was DP-type spin relaxation ($\tau_{so} \propto \tau_p^{-1}$) instead of EY-type spin relaxation ($\tau_{so} \propto \tau_p$). Note that the slope of the red dashed line for the metallic films is larger than that of the blue dashed line for the insulating films. The abrupt decrease in τ_{so}^{-1} near MIT was also reported in ultrathin SIO films with $R_s = 3-4$ k Ω below quantum resistance $R_Q = 25$ k Ω , while τ_{so} was governed by the EY mechanism of SIO films [35]. For SNO, the R_s of films with $t = 3.3-4.0$ nm ranged from 3 k Ω to 25 k Ω , and L_p ranged from 0.12 to 0.75 nm, which are close to the value of the lattice constant. Therefore, one explanation for the sudden reduction of τ_{so}^{-1} is a change in the band structure at the MIT. According to the DP spin relaxation mechanism, the relation between τ_{so}^{-1} and τ_p is expressed as [20] [32] [36] [37] [38]:

$$\tau_{so}^{-1} = \frac{1}{2} \left(\frac{\Delta_{so}}{\hbar} \right)^2 \tau_p, \quad (9)$$

where Δ_{so} is the energy band splitting due to SOC and α_R is the Rashba parameter. Δ_{so} was estimated with Eq. (9) and plotted against t in Fig. 3(d) with red and blue circles, corresponding to films in the metallic and insulating regimes, respectively. Thus, the reduction in τ_{so}^{-1} is related to the decrease in Δ_{so} by a factor of approximately 3 at the MIT.

Figure 4 shows α_R at 2 K as a function of t . In the metallic regime, Δ_{so} is related to k_F and α_R with the following expression by assuming a parabolic band structure:

$$\Delta_{so} = 2k_F \alpha_R, \quad (10).$$

We employed k_F calculated from Eq. (3) using an experimental value of n_s , and we obtained α_R from Eq. (10) for films of all thicknesses, although k_F is not a good parameter in the insulator regime. Thus, α_R for films with $t \leq 4.0$ nm is not a very reliable value. The values of α_R for our SNO ultrathin films for all thicknesses were larger than those reported for other ultrathin films of metallic oxides, SrIrO₃ (SIO) (green solid squares) and La_{2/3}Sr_{1/3}MnO₃ (LSMO) (light blue solid triangles), and comparable to or smaller than the values reported for oxide heterointerfaces [14] [15] [16] [18], which are on the order of 10⁻¹² -10⁻¹¹ eV \cdot m. It is expected that α_R can be enhanced by reducing the film thickness, while the MIT at the ultrathin film prevents us from seeing this enhancement. Therefore, we expect that, combined with improved fabrication and a sophisticated carrier doping technique, SNO metallic ultrathin films with a few monolayers will be a promising material system for practical applications in Rashba-based spintronics devices.

In summary, to reveal the spin relaxation mechanism of SNO ultrathin films, the transport properties of a series of films with different t were measured on both sides of the MIT. The MR at 2 K for the films with various t and disorder was analyzed using WAL theory, and it was found that $\tau_{so} \propto \tau_p^{-1}$. This result verified the DP-type spin relaxation mechanism, indicating the dominant Rashba effect. The values of α_R were on the order of 1×10^{-12} eVm, which were largest in the values reported for other ultrathin films of metallic oxides.

This work was supported in part by JSPS KAKENHI (Grant Nos. 21H01038 and 19H02798) and CREST-JST (Grant No. JPMJCR15Q2).

References

- [1] E. I. Rashba, *Fiz. Tverd. Tela (Leningrad)* 2, 1224 (1960) [*Sov. Phys. Solid State* 2, 1109 (1960)].
- [2] E. I. Rashba and Yu. A. Bychkov, *J. Phys. C* 17, 6039 (1984).
- [3] R. Winkler, *Spin-Orbit Coupling Effects in Two-dimensional Electron and Hole Systems* (Springer Tracts in Modern Physics) Vol. 191 (Berlin: Springer) (2003).
- [4] A. Manchon, H. C. Koo, J. Nitta, S. M. Frolov, and R. Duine, *Nat. Mater.* 14, 871 (2015).
- [5] A. Soumyanarayanan, N. Reyren, A. Fert, and C. Panagopoulos, *Nature* 539, 509 (2016).
- [6] A. B. Yu, and E. I. Rashba, *J. Phys. Condens. Matter* 17, 6039 (1984).
- [7] J. Sinova, D. Culcer, Q. Niu, N. A. Sinitsyn, T. Jungwirth, and A. H. MacDonald, *Phys. Rev. Lett.* 92, 126603 (2004).
- [8] S. Datta and B. Das, *Appl. Phys. Lett.* 56, 665 (1990).
- [9] H. C. Koo, J. H. Kwon, J. Eom, J. Chang, S. H. Han, and M. Johnson, *Science* 325, 1515 (2009).
- [10] E. Lesne, Yu Fu, S. Oyarzun, J. C. Rojas-Sánchez, D. C. Vaz, H. Naganuma, G. Sicoli, J.-P. Attané, M. Jamet, E. Jacquet, J.-M. George, A. Barthélémy, H. Ja rès, A. Fert, M. Bibes and L. Vila, *Nat. Mater.* 15, 1261 (2016).
- [11] J. C. Rojas Sánchez, L. Vila, G. Desfonds, S. Gambarelli, J. P. Attané, J. M. De Teresa, C. Magén and A. Fert, *Nat. Commun.* 4, 2944 (2013).
- [12] J.-C. Rojas-Sánchez, S. Oyarzún, Y. Fu, A. Marty, C. Vergnaud, S. Gambarelli, L. Vila, M. Jamet, Y. Ohtsubo, A. Taleb-Ibrahimi, P. Le F`evre, F. Bertran, N. Reyren, J.-M.

- George, and A. Fert, *Phys. Rev. Lett.* 116, 096602 (2016).
- [13] J. Sinova, S. O. Valenzuela, J. Wunderlich, C. H. Back, T. Jungwirth, *Rev. Mod. Phys.* 87, 1213 (2015).
- [14] A. D. Caviglia, M. Gabay, S. Gariglio, N. Reyren, C. Cancellieri, and J. M. Triscone, *Phys. Rev. Lett.* 104, 126803 (2010).
- [15] M. J. Veit, R. Arras, B. J. Ramshaw, R. Pentcheva, and Y. Suzuki, *Nat. Commun* 9, 1458 (2018).
- [16] W. Lin, L. Li, F. Dogan, C. Li, H. Rotella, X. Yu, B. Zhang, Y. Li, W. S. Lew, S. Wang, W. Prellier, S. J. Pennycook, J. Chen, Z. Zhong, A. Manchon, and T. Wu, *Nat. Commun.* 10, 3052 (2019).
- [17] N. Wadehra, R. Tomar, R. M. Varma, R. K. Gopal, Y. Singh, S. Dattagupta and S. Chakraverty, *Nat. Commun* 11, 874 (2020).
- [18] N. Kumar, N. Wadehra, R. Tomar, Shama, S. Kumar, Y. Singh, S. Dattagupta, S. Chakraverty, *Adv. Quantum. Technol.* 4, 2000081 (2021).
- [19] L. Zhang, Y. B. Chen, B. Zhang, J. Zhou, S. Zhang, Z. Gu, S. Yao, and Y. F. Chen, *J. Phys. Soc. Jpn* 83, 054707 (2014).
- [20] S. P. Chiu, M. Yamanouchi, T. Oyamada, H. Ohta, and J. J. Lin, *Phys. Rev. B* 96, 085143 (2017).
- [21] D. Oka, Y. Hirose, S. Nakano, T. Fukumura, and T. Hasegawa *Phys. Rev. B* 92, 205102 (2015).
- [22] Y. Park, D. Oka, Y. Hirose, T. Hasegawa, and R. Engel-Herbert et al., *Commun. Phys.* 3, 102 (2020).
- [23] J. M. Ok, N. Mohanta, J. Zhang, S. Yoon, S. Okamoto, E. S. Choi, H. Zhou, M. Briggeman, P. Irvin, A. R. Lupini, Y. Y. Pai, E. Skoropata, C. Sohn, H. Li, H. Miao, B. Lawrie, W. S. Choi, G. Eres, J. Levy, H. N. Lee, *Sci. Adv.* 7, 38, eabf9631 (2021)..
- [24] H. Jin, K. Lee, S.-H. Baek, J.-S. Kim, B. Cheong, B. H. Park, S. Yoon, B. J. Suh, C. Kim, S. S. A. Seo, and S. Lee, *Sci. Rep.* 6, 34295 (2016).
- [25] S. W. Cho, M. Lee, S. Woo, K. Yim, S. Han, W. S. Choi and S. Lee, *Sci. Rep.* 8, 5739 (2018).
- [26] J. Fabian and S. D. Sarma, *J. Vac. Sci. Technol. B* 17, 1708 (1999).
- [27] R. B. Macquart, B. J. Kennedy, and M. Avdeev, *J. Solid State Chem.* 183, 2400 (2010).
- [28] See Supplemental Material at [URL] for [contents].
- [29] "S. Hikami, A.I. Larkin, Y. Nagaoka, *Prog. Theor. Phys.* 63 707 (1980)".

- [30] S. X. Zhang, R. D. McDonald, A. Shekhter, Z. X. Bi, Y. Li, Q. X. Jia, and S. T. Picraux, *Appl. Phys. Lett.* 101, 202403 (2012).
- [31] "Iordanskii, Lyanda-Geller, and Pikus, *JETP Lett.* 60, 206 (1994)".
- [32] W. Knap, C. Skierbiszewski, A. Zduniak, E. Litwin-Staszewska, D. Bertho, F. Kobbi, J. L. Robert, G. E. Pikus, F. G. Pikus, S. V. Iordanskii, V. Mosser, K. Zekentes, and Yu. B. Lyanda-Geller, *Phys. Rev. B* 53, 3912 (1996).
- [33] B. L. Altshuler, A. G. Aronov, and D. E. Khmel'nitsky *J. Phys. C* 15, 7367 (1982).
- [34] S. Chakravarty and A. Schmid, *Phys. Rep.* 140, 193 (1986).
- [35] L. Zhang, X. Jiang, X. Xu, and X. Hong, *APL Mater.* 8, 051108 (2020).
- [36] M. I. D'yakonov and V. I. Perel', *J. Exp. Theor. Phys.* 33, 1053 (1971).
- [37] T. Koga, J. Nitta, T. Akazaki, and H. Takayanagi, *Phys. Rev. Lett.* 89, 046801 (2002).
- [38] C. Schierholz, T. Matsuyama, U. Merkt, and G. Meier, *Phys. Rev. B* 70, 233311 (2004).

Supplementary Material

Large Rashba parameter for 4d strongly correlated perovskite oxide SrNbO₃ ultrathin films

Hikaru Okuma*, Yumiko Katayama, and Kazunori Ueno

Department of Basic Science, University of Tokyo,

Meguro, Tokyo 153-8902, Japan

*hikaruokuma613@g.ecc.u-tokyo.ac.jp

A. Fitting to HLN theory taking into account the EY spin-relaxation mechanism

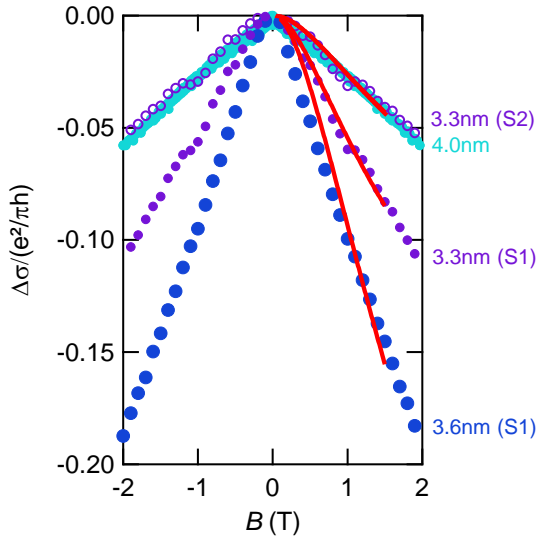


FIG. S1. $\Delta\sigma = \sigma(B) - \sigma(0)$ in units of $e^2/\pi\hbar$ measured in the perpendicular magnetic field B for films with t ranging from 3.3 nm to 4.0 nm at 2 K. The red solid lines are fits to the data based on HLN theory [Eq. (1)].

Figure S1 shows $\Delta\sigma(B)$ at 2 K and the fitting of the data to HLN theory [Eq. (1)] taking into account the EY spin-relaxation mechanism. $\Delta\sigma(B)$ for films with $t = 3.3$ (S1), 3.3 (S2), and 4.0 nm followed Eq. (1). However, $\Delta\sigma(B)$ for film with $t = 3.6$ nm (S1) deviated from the fit over a low B range, and for films with $t = 5.5$ -8.5 nm and 3.6 nm (S2), $\Delta\sigma(B)$ did not follow Eq. (1) (not shown here). Thus, the values of L_p deduced from the fitting of the data for the films with $t = 3.3$ (S1), 3.3 (S2), 3.6 (S1), and 4.0 nm were 20.4, 17.9, 19.4, and 17.5 nm, and those obtained from k_F and μ were 0.75, 0.44, 0.60, and 0.15 nm, respectively. Notably, the values of L_p deduced from the fitting were nearly two orders of magnitude larger

than those obtained from k_F and μ . Therefore, it is unlikely that the B dependence of the MR is explained by HLN theory taking into account the EY spin-relaxation mechanism.

B. Fitting to ILP theory taking into account the DP spin-relaxation mechanism

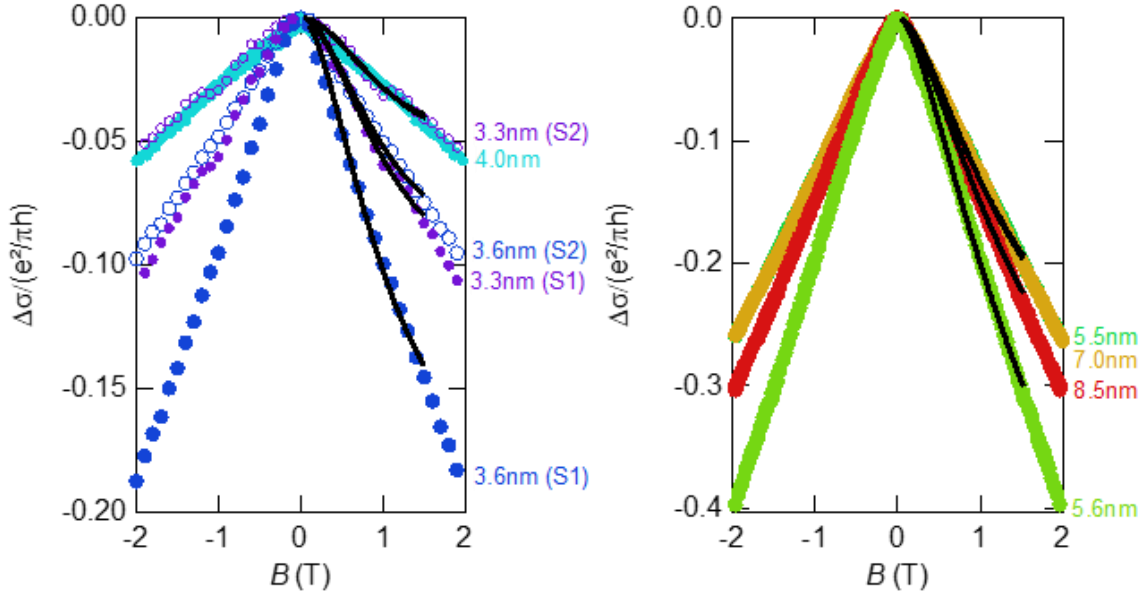


FIG. S2. $\Delta\sigma=\sigma(B)-\sigma(0)$ in units of $e^2/\pi\hbar$ measured in the perpendicular magnetic field B for films with t ranging from 3.3 to 4.0 (left) and 5.5 nm to 8.5 nm (right) at 2 K. The black solid lines are fits to the data based on ILP theory [Eq. (4)].

Figure S2 shows $\Delta\sigma(B)$ at 2 K and the fitting of the data to Iordanskii-Lyanda-Pikus (ILP) theory [Eq. (4)] taking into account the DP spin-relaxation mechanism. $\Delta\sigma(B)$ follows Eq. (4) for films with t ranging from 3.3 to 8.5 nm.

